PHOTONICS Research

Lithium niobate micro-waveguides for efficient supercontinuum generation and frequency comb self-referencing

YONGZHI TANG,^{1,2} D JING QIU,^{1,3} WENJUN DING,¹ TINGTING DING,⁴ XINGZE SONG,¹ D TIANHAO XIAN,¹ HAO LI,¹ SHIJIE LIU,¹ LUQI YUAN,¹ D YUANLIN ZHENG,^{1,3,5,7} D AND XIANFENG CHEN^{1,3,5,6,8}

¹State Key Laboratory of Photonics and Communications, School of Physics and Astronomy, Shanghai Jiao Tong University, Shanghai 200240, China

²MOE Key Laboratory of Weak-Light Nonlinear Photonics, TEDA Institute of Applied Physics and School of Physics, Nankai University, Tianjin 300457, China

Received 28 May 2025; revised 20 July 2025; accepted 26 August 2025; posted 26 August 2025 (Doc. ID 568903); published 20 November 2025

Optical frequency combs (OFCs) and supercontinuum generation (SCG) facilitate a plethora of important applications in metrology, spectroscopy, optical clocks, etc. Recent advances in integrated photonics offer an attractive avenue to implement compact or chip-integrated comb sources. However, the prevalent method based on nano-waveguides usually exhibits low output power and large coupling losses during the SCG process. Here, we experimentally demonstrate over two-octave-spanning SCG with high output power in dispersion-engineered magnesium-oxide-doped lithium-niobate-on-insulator (MgO:LNOI) micro-waveguides using a high-repetition-rate femtosecond fiber oscillator laser. The micro-waveguide can deliver high-power SCG due to its excellent fiber compatibility, lower insertion loss, and higher optical damage threshold. The designed waveguide also allows for birefringence phase matched second-harmonic generation (SHG), realizing simultaneous f-2f interference in a single-pass configuration. Measurement and stabilization of carrier-envelope offset frequency (f-CEO) are achieved with over 36-dB signal-to-noise ratio for OFC self-referencing. Furthermore, a nonlinear envelope equation model is established to simulate the spectral broadening and frequency conversion process regarding cascaded $\chi^{(2)}$ and $\chi^{(3)}$ nonlinearities. This work provides a compact and convenient solution for f-2f self-referencing frequency combs using photonic micro-waveguide technology.

https://doi.org/10.1364/PRJ.568903

1. INTRODUCTION

Optical frequency combs (OFCs) are a set of teeth-shaped spectral lines with equidistant frequency spacing and phase coherence, which have successfully connected optical frequencies to radio frequencies with extremely precise frequency intervals, and have broad application prospects in high-precision metrology fields such as astronomical spectral calibration, optical atomic clocks, and frequency measurement [1–8]. Significant spectral broadening via supercontinuum generation (SCG) is crucial for achieving self-referencing and forming stable OFCs. The generation of a coherent octave-spanning supercontinuum allows for the determination of $f_{\rm CEO}$ through self-referenced f-2f interference, thereby enabling the realization of ultrastable frequency combs [9,10]. Fundamentally, it

represents a pathway to acquiring ultra-broadband coherent comb sources.

An optical time soliton is generated by the balance of a non-linear effect and dispersion when an ultrafast light pulse propagates in a nonlinear medium. Soliton induced resonance radiation (RR) plays an important role in the generation of supercontinuum [11,12], realizing spectral broadening and time compression. RR waves, generated in the four-wave mixing process through third-order nonlinear ($\chi^{(3)}$) Kerr self-phase modulation, are also called dispersive waves. They can coherently promote the expansion of supercontinuum bandwidth. Previous studies have shown that there is a novel type RR wave in quadratic media, that is, RR waves generated by solitons through a three-wave mixing (3WM) process dominated by

³Zhangjiang Laboratory, Shanghai 201210, China

⁴School of Electronic and Electrical Engineering, Shanghai University of Engineering Science, Shanghai 201620, China

⁵Shanghai Research Center for Quantum Sciences, Shanghai 201315, China

⁶Collaborative Innovation Center of Light Manipulations and Applications, Shandong Normal University, Jinan 250358, China

⁷e-mail: ylzheng@sjtu.edu.cn

⁸e-mail: xfchen@sjtu.edu.cn

the second-order nonlinearity $(\chi^{(2)})$ [13–15]. Early studies on OFCs and SCG are mainly based on highly nonlinear or photonic crystal fibers with $\chi^{(3)}$ nonlinearity [11,16], which usually rely on additional $\chi^{(2)}$ nonlinear material, e.g., lithium niobate (LN), for second-harmonic generation (SHG) to achieve f-2fself-referencing [17,18]. However, these methods completely separate $\chi^{(2)}$ and $\chi^{(3)}$ nonlinear processes and are not conducive to device integration. Besides, extra delay lines or dispersion compensating fibers are usually used to compensate for the dispersion walk-off, which also increases system complexity, raises costs, and limits stability. Significant advances in micro and nano manufacturing technology have facilitated the development of a variety of integrated photonic platforms, including silicon, silicon nitride, and aluminum nitride [19-24]. Although significant progress has been made in OFC research in the near-infrared region, there remains a lack of highly efficient, widely frequency-covered, and tunable comb sources, especially in the visible regions [25]. Integrated waveguides are expected to further address light field limitations and make it possible to utilize efficient SCG and self-referencing on a single chip to get OFCs, which allows for greater flexibility, compactness, and scalability of portable OFC devices. Lithium niobate, also dubbed as the "silicon of photonics", is an excellent multifunctional crystal with comprehensive performance due to its wide transparent window, high refractive index, high electro-optical coefficient, and large nonlinear coefficient. The development of lithium-niobate-on-insulator (LNOI) addresses the challenges associated with traditional LN-based optical integration [26-28], supporting precise dispersion engineering and strict waveguide mode constraints. Synchronous detection of $f_{\rm CEO}$ on a chip is achievable through cascaded $\chi^{(2)}$ and $\chi^{(3)}$ nonlinear processes [29–32], which revolutionizes the traditional method of conducting SCG and SHG processes separately.

In recent years, there have been many SCG studies based on LN nano-waveguides [33-37]. The advantage of nano-waveguides is that the effective mode area is small, so high normalized nonlinearity can be obtained. However, there are some challenges that are not easy to overcome. First of all, the strong dispersion of the nano-waveguide makes the refractive index very sensitive to small deviations in the structure and greatly affects the bandwidth and flatness of the SCG spectrum [37,38], so high precision is required in the fabrication. Additionally, the compatibility of nano-waveguides with standard single-mode fibers remains inadequate due to the serious mode mismatch. The ultrawide spectral spanning of SCG makes it difficult for efficient light coupling even by integration of couplers or spot size converters [34-40]. It also greatly increases the fabrication complexity and cost [41,42]. Besides, based on the third-order nonlinear SCG process, the peak power of the required pumped pulsed light is usually inversely proportional to the length of the device. But nano-waveguides are limited in length (typically shorter than 2 cm) due to constraints of electron beam lithography [36,39,40], so the power requirement for a pumped pulse is increased. In summary, the SCG and OFCs based on nano-waveguides are solely limited to laboratory conditions because of the above problems, and they are difficult to meet high-power application scenarios.

Conversely, the dispersion-engineered LNOI micro-waveguide effectively solves the above problems. The LNOI micro-waveguides intrinsically match well with fiber, which facilitates compatibility with fiber-optic devices [43-45]. The transmittance can be improved to 70% with anti-reflection coating. Besides, previous studies show that the dispersion of the micro-waveguide is much flatter than that of nano-waveguides in a wide range in the communication bands [34], which is beneficial in obtaining flat SCG and robustness against structural variation. Micro-waveguides fabricated by UV lithography technology and direct femtosecond (fs) laser writing technology have no limitation on waveguide length and have significant advantages in low-cost and scalable production [44-47]. Lastly, the threshold for optical damage is a crucial consideration in high-power SCG; the MgO-doped microwaveguides also exhibit superior resistance to optical damage compared to nano-waveguides [45,48,49].

Here, we experimentally obtain efficient over-two-octave SCG in dispersion managed MgO:LNOI ridge micro-waveguides, which are pumped by a femtosecond fiber oscillator laser centered at the telecommunication band. By leveraging excellent fiber compatibility of the micro-waveguide, high coupled-to-fiber SCG power is obtained. Theoretical modeling using a single nonlinear envelope equation with contributions from both $\chi^{(2)}$ and $\chi^{(3)}$ nonlinearities reveals various cascaded nonlinear phenomena in the SCG process. We theoretically investigate the evolution of supercontinuum spectral broadening with increasing pump power and propagation distance, which agrees well with the experimental results. Tunable SCG and SHG are simultaneously observed, and the spectral overlap is achieved near the 1 µm band. We demonstrated on-chip f-2f interferometry by utilizing spectral overlap between the simultaneous SCG and SHG, enabling direct detection of the carrier-envelope offset frequency of the pump source, thus offering the potential to produce a self-referenced OFC.

Figure 1 conceptually illustrates the generation and evolution of a supercontinuum spectrum in the MgO:LNOI microwaveguide. The supercontinuum is generated and gradually

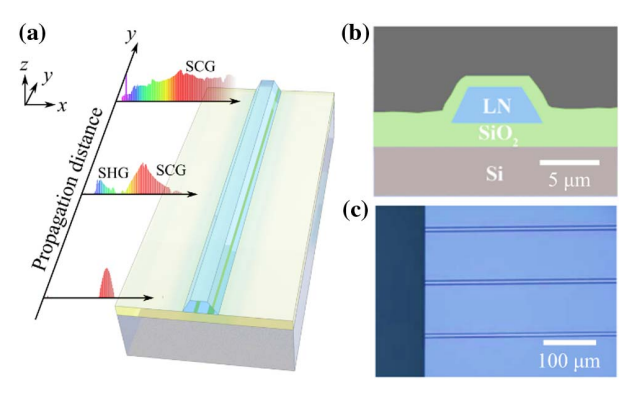


Fig. 1. LNOI micro-waveguides for SCG and frequency comb selfreferencing. (a) Schematic illustration of SCG and SHG in a MgO: LNOI micro-waveguide for f-2f self-referenced OFC. The optical axis of LN is along the z axis. The direction of light propagation is the γ axis of LN. (b) SEM image of the waveguide cross section. (c) Optical microscopic image of the micro-waveguides.

broadened in the 2-cm-long z-cut MgO:LNOI micro-waveguide, and finally overlaps with the SHG spectrum, which allows for the detection of f_{CEO} through f-2f interferometry, thereby enabling a stabilized frequency comb. In the experiment, the waveguide is fabricated from a commercial LNOI wafer (NanoLN) with a 3-µm-thick z-cut MgO-doped LN layer bonded on top of a 2-µm-thick silica buffering layer on a 500-µm Si substrate. A scanning electron microscope (SEM) image of the micro-waveguide cross section is shown in Fig. 1(b). The top width of the ridge waveguide is 3.6 µm. In fact, a series of waveguides with top-widths gradually increasing starting from 2.6 to 4.6 µm at 0.2 µm intervals is fabricated. The LNOI layer is fully etched [see also Fig. 1(b)], and the etching sidewall angle is 62°. Then a layer of SiO₂ is deposited on top to form the fully buried MgO:LNOI microwaveguide. Figure 1(c) shows the optical microscope image of the fabricated micro-waveguide sample. The ends of the waveguides are finely polished to facilitate light coupling.

2. THEORY AND SIMULATION

In order to simulate the SCG process, the time-domain non-linear Schrodinger equation for cascaded quadratic and cubic nonlinearities [50,51] is established as follows:

$$\begin{split} & \left[\frac{\partial}{\partial y} + \frac{\alpha}{2} - \sum_{n=2,3,\dots} \frac{i^{n+1}\beta_n}{n!} \left(\frac{\partial}{\partial T} \right)^n \right] E(y,T) \\ & = \frac{\omega_0^2}{2c^2 \varepsilon_0 \beta(\omega_0)} \left(i - \frac{1}{\omega_0} \frac{\partial}{\partial T} \right) P_{\text{NL}}(y,T), \end{split}$$

where $P_{\rm NL}(y,T)=P_{\rm NL}^{(2)}(y,T)+P_{\rm NL}^{(3)}(y,T)=\varepsilon_0\chi^{(2)}$: $EE+\varepsilon_0\chi^{(3)}$:EEE represents the total nonlinear polarization. In the simulation, the values used for the nonlinear susceptibilities for type-I $\chi^{(2)}$ and $\chi^{(3)}$ are 10 pm·V⁻¹ and 5200 pm²·V⁻², respectively [33]. The amplitude E(y, T) of the evolving pulse is a function of the propagation distance ξ and the delay time defined by $T = t - y/v_{\varrho}$, α is the propagation loss, ω_0 is the pump frequency, and β_n is the *n*-th order dispersion coefficient. The spectral evolution is then simulated by numerically solving the nonlinear envelope equation using the split-step Fourier method [52]. Physically, the soliton region requires anomalous group velocity dispersion (GVD) to balance the nonlinear self-phase modulation (SPM) effect, which allows for effective soliton self-compression and thus spectral coherence broadening. In addition to SPM, high-order dispersion in waveguides can also cause perturbations in soliton dynamics, especially the generation of dispersive waves, which further extends the bandwidth of soliton-based supercontinuum spectra [19]. The phase matching condition between the non-dispersive soliton pulse (frequency center ω_s , group velocity v_g) and dispersive waves is

$$\Delta\beta(\omega) = \beta(\omega) - \beta(\omega_s) - \frac{1}{\nu_g}(\omega - \omega_s) = 0.$$

The integrated dispersion is defined as the sum of higherorder dispersion terms (second-order dispersion and above) $\beta_{\rm int}(\omega) = \sum_{m=2}^{\infty} \frac{(\omega - \omega_0)^m}{m!} \frac{{\rm d}^m}{{\rm d}\omega^m} \beta(\omega_0) = \Delta \beta(\omega)$, where $\beta(\omega)$ is the propagation constant of the wave, $\beta_n(\omega_0)$ corresponds to the *n*-th order dispersion coefficient, ω_0 is the pump central

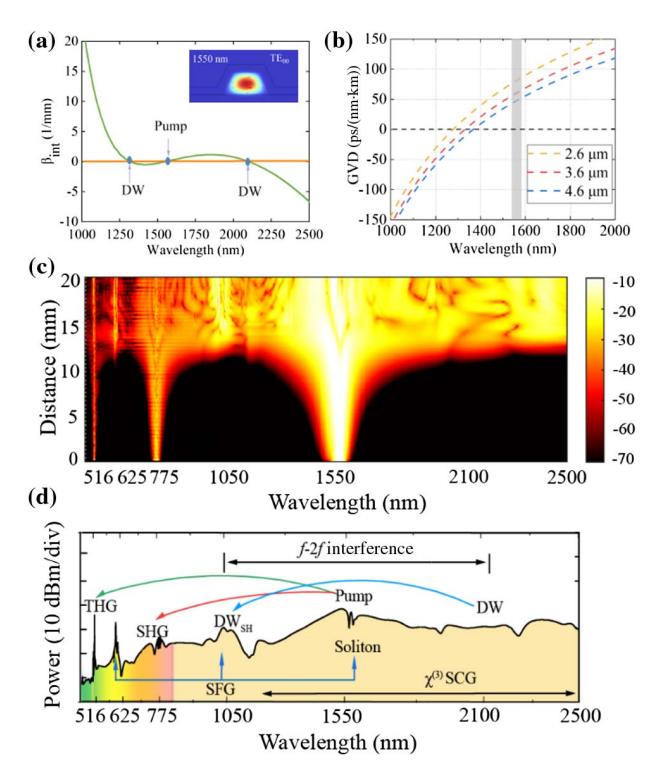


Fig. 2. Simulation of SCG in LNOI micro-waveguides. (a) Simulated integrated dispersion corresponding to the TE_{00} mode in the 3.6- μ m-wide waveguide. Inset: TE_{00} mode profile at 1550 nm. (b) Simulated GVD for different top-width waveguides. The gray area indicates the position of the pulsed light pumped. (c) Spectral broadening and evolution of fs pulses in the 2-cm-long waveguide. (d) Simulated supercontinuum spectrum at the micro-waveguide output and the schematic diagram of cascading nonlinear process.

frequency, and v_{q} is the group velocity at the pump frequency. The case of integral dispersion β_{int} equal to zero indicates that the phase matching condition for the generation of dispersive waves is satisfied. The micro-waveguide dispersion is simulated using a finite-difference method (FDM) mode solver. The pump light mode is chosen to be TE fundamental mode to enable broadband SCG and type-I birefringent phase matching (BPM) SHG in the z-cut LNOI micro-waveguide. The inset of Fig. 2(a) shows the calculated TE_{00} mode profile at 1550 nm. Figure 2(a) shows the simulated β_{int} curve corresponding to the TE₀₀ mode at the 3.6-µm-wide waveguide. Figure 2(b) shows the simulated group velocity dispersion (GVD) curves. The waveguide is designed with flat and moderate anomalous dispersion near the central wavelength of 1550 nm to balance the nonlinear SPM effect, thus enabling soliton self-compression to generate an efficient supercontinuum. The GVD curve of the micro-waveguide rises monotonically with the increasing wavelength, so there is only one zero dispersion wavelength. Unlike the nano-waveguide, whose dispersion is highly sensitive to even small variations in the waveguide structure parameters [37], the micro-waveguide inherently possesses greater robustness against them.

Figures 2(c) and 2(d) show the spectral evolution simulation results when the femtosecond pulse propagates in the 2-cm-long MgO:LNOI micro-waveguide. In the simulation,

the 1550-nm fs pump pulse is 1.65 kW in pump power with a pulse energy of 988 pJ. The waveguide has a top width of 3.6 µm and an etching depth of 3.0 µm. Various nonlinear processes have been taken into consideration, including cascaded second- and third-order nonlinearities, cascaded second- and third-order nonlinear effects, as well as the effects of higher-order dispersion and self-steepening. Figure 2(c) shows the results of spectral broadening and evolution of pulsed light with the propagation distance in the waveguide. SHG and third-harmonic generation (THG) processes immediately occur (SHG at the central wavelength of 775 nm and THG at 516.6 nm) when pulsed light is fed into the waveguide. Notably, there exists an interplay between the second- and third-order processes throughout the entire propagation, which collectively leads to a significant broadening of the initial spectrum. Additionally, the second and third harmonics cascade with the fundamental harmonic [50,53], competing with the effects of third-order nonlinearity. The $\chi^{(3)}$ nonlinear process dominates when $z \le 12$ mm. Under the combined effect with dispersion, the spectrum is broadened and the pulse is compressed. The RR wave takes the form of a dispersive wave (DW). Because the phase matching condition of the four-wave mixing process is satisfied, strong DW appears at 2100 nm. The spectral position of DW is predicted from the zero-crossing of the integrated dispersion in Fig. 2(a). The supercontinuum spectrum is fully broadened when z = 12 mm, and in the subsequent waveguide lengths ($z \ge 12$ mm), the cascaded secondorder nonlinearity process gradually becomes dominant, further promoting the expansion of the supercontinuum bandwidth through the 3WM process. The BPM SHG process occurs to convert the DW wavelength from 2100 to 1050 nm. As the propagation distance increases, the SCG and SHG spectra further broaden and overlap, so the f-2f interference to measure $f_{\rm CEO}$ can be achieved on a single chip. Notably, a clear signal is observed near 626 nm in the simulated spectrum, which is generated by the sum-frequency generation (SFG) process between optical solitons at 1550 nm and the second harmonic of DW near 1050 nm, extending the RR wave into the visible light range. This work observes the phenomenon of time solitons inducing RR wave generation through the 3WM process in LNOI micro-waveguides, a mechanism previously reported in bulk quadratic nonlinear crystals [15]. Compared with bulk crystals, our study shows that dispersion can be flexibly engineered by adjusting waveguide geometry on integrated photonic platforms, enabling precise control of 3WM phase matching conditions. This will provide a new degree of freedom for regulating soliton-resonant radiation interactions. Under the condition of pulsed light input at the central wavelength of 1550 nm, the simulated SCG spectrum at the waveguide output (z = 20 mm) is shown in Fig. 2(d). The schematic diagram of the cascaded nonlinear process is presented. According to our design, the dispersion engineering of the waveguide allows for the generation of strong DWs near 2 μm. Meanwhile, the SHG from 2 to 1 μm is achieved through natural type I BPM, without an additional poling technique. Next, we simulate in detail the change of the BPM wavelength and predict the position of the DWs in the spectrum during the SCG process with the variation of the waveguide

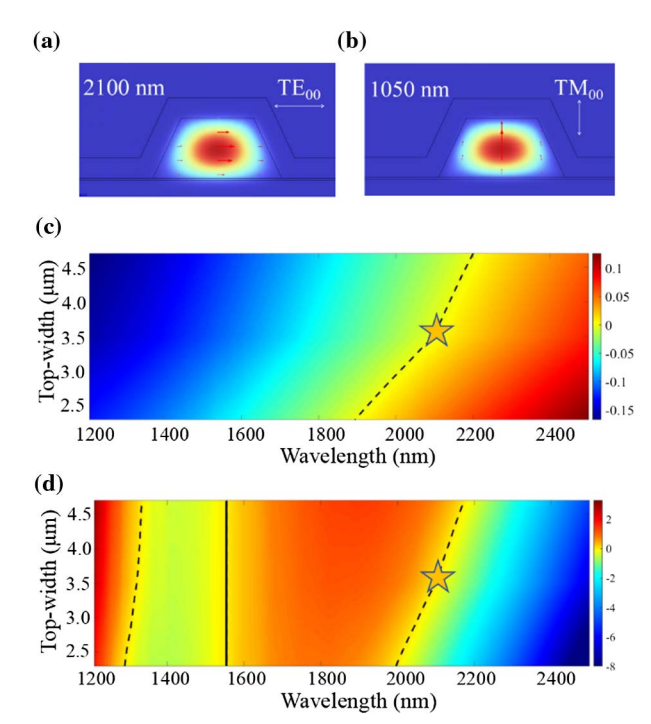


Fig. 3. Simulated spectral positions of DWs generation and BPM SHG under different waveguide widths. (a) Calculated TE_{00} mode profile at 2100 nm. (b) Calculated TM_{00} mode profile at 1050 nm. (c) Variation of the phase mismatch Δk with the waveguide top-width. The dashed line indicates the phase matching condition. (d) Variation of the integrated dispersion $\Delta \beta$ with the waveguide top-width. The solid line shows the central wavelength of the pulsed light; the dashed line predicts the DW generation.

width parameter. Figures 3(a) and 3(b) show the calculated TE_{00} and TM_{00} mode profiles of the waveguide at 2100 and 1050 nm. Figure 3(c) shows the variation of SHG phase mismatch Δk corresponding to different waveguide widths, and the dashed line indicates $\Delta k = 0$, that is, the phase matching condition. As the waveguide width increases from 2.6 to 4.6 µm, the SHG matching wavelength increases from 1900 to 2200 nm. Figure 3(d) shows the integrated dispersion $\Delta\beta$ variation with different waveguide widths. The solid black line indicates the wavelength of the optical soliton and the dashed line corresponds to $\Delta \beta = 0$, that is, the condition for the generation of DWs. When the waveguide width increases from 2.6 to 4.6 µm, the wavelength range of long-wavelength DW shifts from 2000 to 2180 nm. It is observed that when the waveguide width is 3.6 µm, the central wavelength of the DW coincides with the BPM SHG at 2100 nm, which is indicated by the star symbol in the figure. Under this waveguide configuration, the frequency doubling signal of dispersive wave DWSH is the strongest, which ensures spectral overlap between the SCG and SHG near 1050 nm, enabling strong $f_{\rm CEO}$ beatnote generation for self-referencing.

3. EXPERIMENT AND DISCUSSION

The experimental setup is depicted in Fig. 4(a). The pump source is a mode-locked femtosecond fiber oscillator laser centered at 1550 nm (average power 110 mW, pulse duration

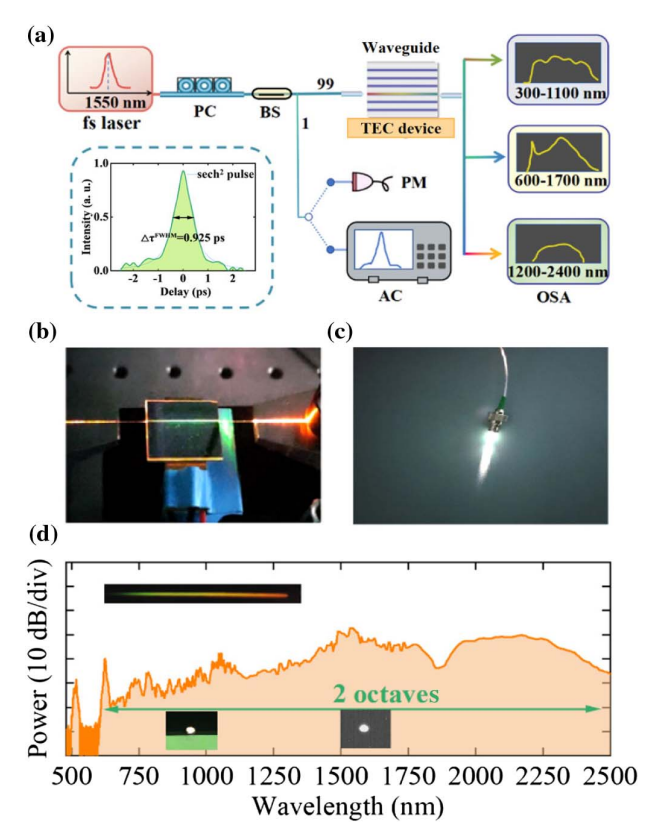


Fig. 4. SCG experiments in the MgO:LNOI micro-waveguide. (a) Diagram of the experimental setup and autocorrelation measurement result of the sech² shape fs pulse at the input of the waveguide. (b) Photograph of scattered SCG and SHG in the micro-waveguide. (c) Bright white light at the output of the waveguide collected with an optical fiber. (d) Experimental supercontinuum spectrum spanning two octaves. The insets show the dispersed spectrum of SCG and fundamental mode profiles of pump and SCG.

~100 fs, repetition rate 80 MHz). The polarization state of the incident laser is adjusted to be TE mode by a polarization controller (PC) and the light is coupled into and out of the micro-waveguide via the end coupling method using a pair of polarization-maintaining lensed fibers. The temperature of the micro-waveguide sample is controlled by a thermoelectric cooler (TEC) device, set at 25°C in the experiment. We use a 1:99 beam splitter (BS) behind the laser to facilitate power detection using a photodiode (PD) and pulse width measurement using an autocorrelator (AC). The spectrum of the waveguide output is recorded using three optical spectral analyzers (OSAs) with different measuring ranges, covering 300-1100 nm, 600-1700 nm, and 1200-2400 nm. The inset of Fig. 4(a) shows the autocorrelation function (ACF) signal of the input fs pulse at the input end of the micro-waveguide, showing a full width at half maximum (FWHM) of 925 fs. The actual FWHM of the pulse width is ~600 fs assuming a sech2 type temporal waveform of the pulse. Figure 4(b) shows the experimentally observed SCG and harmonic generation result in the 2-cmlong MgO:LNOI micro-waveguide. The 1550-nm fs pulsed laser is injected into the waveguide from the left side through the lensed fiber. The bright visible light including orange-red

and green light in the waveguide is produced by the SHG, SFG, and THG processes. Figure 4(c) shows a photograph of the collected light from the waveguide's output end in bright white color. Experimentally, we use 1550-nm continuous wave (CW) light to estimate the insertion loss of the micro-waveguide, which is 3.4 dB for TE and 4.1 dB for TM input. The propagation loss is 0.3 dB/cm and 0.4 dB/cm for TE and TM modes, as evaluated by the Fabry-Perot (F-P) interference method. The coupling loss of TE mode between the fiber and waveguide at 1550 nm is deduced to be about 1.4 dB/facet. When utilizing an average power of 110 mW pulsed light TE mode for pumping, the coupled power into the waveguide is 79 mW, corresponding to a peak power of 1.65 kW and a pulse energy of 988 pJ. From the SCG spectrum as shown in Fig. 4(d), it can be seen that the spectrum of the pulsed light has been fully broadened and most of the pump energy has been converted into SCG in the waveguide. Therefore, it can be approximately considered that the energy collected from waveguide output is supercontinuum energy. Therefore, we experimentally obtained a broadband SCG spectrum with pulse energy of 628 pJ, covering the band from near-infrared to visible light. The 30-dB spectral bandwidth exceeds two octaves, ranging from 600 to 2500 nm. The upper left inset in Fig. 4(d) shows a photograph of the visible spectrum after dispersing the collimated output with a diffraction grating and the lower insets show the observed fundamental mode profiles of the pump and SCG.

Figures 5(a) and 5(b) respectively show the evolution of the experimentally measured and theoretically simulated SCG spectra with respect to the pump pulse energy, which are in good agreement. The optical microscope image of the waveguide end face used in the experiment is shown in the inset of Fig. 5(a). The waveguide top-width is 3.6 µm. When the input power is 25.6 mW, the on-chip power is 18.4 mW, and the corresponding pulse energy is 230 pJ, a weak spectral broadening of the fundamental wave, along with SHG and THG, is observed. As the energy further increases to 485 pJ, the SCG and SHG spectra gradually broaden and overlap. For 720 pJ of pulse energy, DW is generated near 2100 nm. According to our design, the BPM SHG process converts the DW wavelength from 2100 to 1050 nm. In addition, we also observe the 626-nm optical signal generated by the SFG process between soliton and the converted 1050-nm DW. Due to cascaded $\chi^{(2)}$ and $\chi^{(3)}$ nonlinearities, the spectrum reflects multiplex nonlinear interactions. When the pulse energy in the waveguide is 988 pJ, SHG and SFG cover the visible spectrum, and together with SCG, a broadband SCG spectrum from the visible to the near infrared is obtained, with a 30-dB bandwidth of 375 THz. It is worth mentioning that it seems that the pulse energy required by the micro-waveguide is larger than that of nano-waveguides, but its effective mode area is an order of magnitude larger, so the pulse energy density required per unit area is comparable. In addition, micro-waveguides can easily obtain high-power SCG due to the advantages of excellent fiber compatibility, flat dispersion, low insertion loss, and high light damage threshold, which present many advantages in realistic applications.

The coherent octave spanning supercontinuum allows detection of $f_{\rm CEO}$ by a self-referencing method, thus achieving

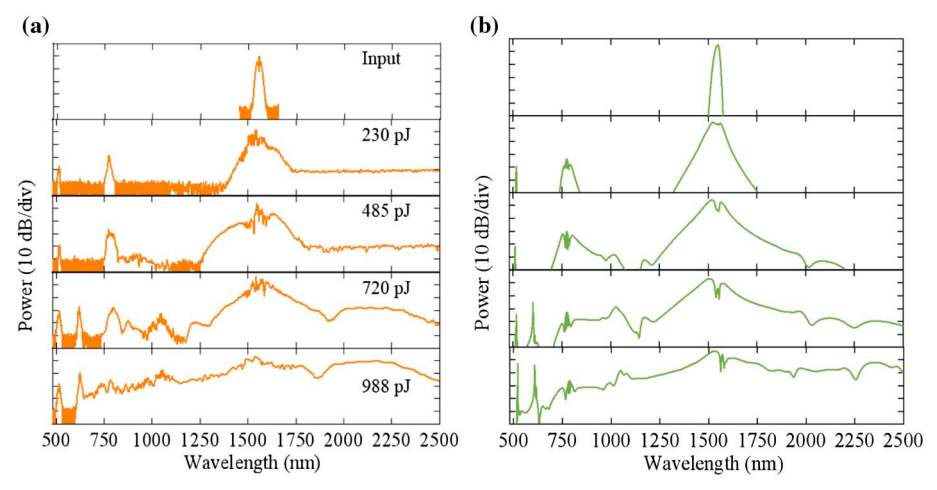


Fig. 5. (a) Experimental and (b) simulated spectral evolutions of SCG with different pump powers.

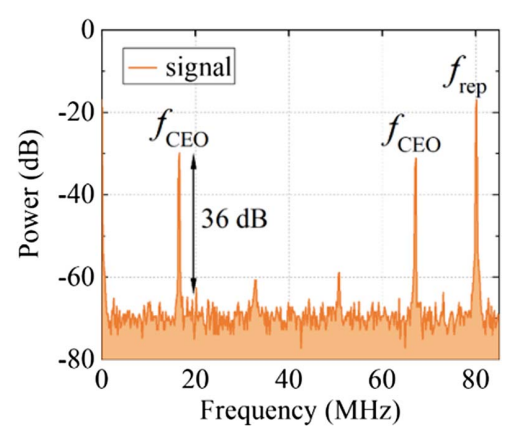


Fig. 6. Experimentally measured frequency comb offset beatnote in the frequency domain.

a stable frequency comb. Directly detecting $f_{\rm CEO}$ in a single waveguide is a compact and convenient scheme. A bandpass filter near the 1-µm band is used to filter out the components of the spectral overlap between SCG and SHG. We then use a high-speed photodiode to detect the signal with an oscilloscope and a spectrum analyzer. The measured $f_{\rm CEO}$ signal in the frequency domain is shown in Fig. 6. An $f_{\rm CEO}$ beatnote with a high signal-to-noise ratio (SNR) of 36 dB is achieved, which is sufficient for further frequency comb locking.

4. CONCLUSION

We demonstrate a two-octave optical bandwidth SCG scheme based on dispersion-engineered LNOI ridge micro-waveguides. Under the femtosecond laser pumping, a high-power supercontinuum spectrum ranging from visible light to near infrared is generated. We investigate the tunable dispersion wave generation and SHG processes in different cross-section sized micro-waveguides, and the theoretical and experimental results agree well. The spectral overlap between broadband SCG and SHG allows the measurement of $f_{\rm CEO}$ in a single waveguide for

frequency comb self-referencing. Compared with nano-wave-guides, LNOI micro-waveguides have excellent fiber compatibility, flatter dispersion, low insertion loss, low fabrication cost, etc., which will provide new opportunities for nonlinear photonics research and applications on the micrometer-thick LNOI platform.

APPENDIX A: RESEARCH RESULTS FOR DIFFERENT WAVEGUIDE WIDTHS

In order to investigate the influence of waveguide top-width on the supercontinuum spectrum, we study the dispersion of waveguides and perform SCG experiments on waveguides of different widths on the same chip. Figures 7(a) and 7(b) show the simulation results of integrated dispersion β_{int} and phase mismatch Δk for waveguide widths of 2.6, 3.6, and 4.6 μ m. With the increase of waveguide width, the β_{int} curve slightly redshifts but the overall contour of the curve remains unaltered. The phase mismatch Δk curve also moves towards longer wavelengths, and the position of $\Delta k = 0$ indicates the BPM SHG process. We experimentally use the same modelocked femtosecond fiber laser (central wavelength 1550 nm, average power 110 mW, pulse duration ~100 fs, repetition frequency 80 MHz) as the pump source. The inset of Fig. 7(c) displays the optical microscope image of the waveguide end face, indicating that the actual waveguide top-widths are 2.60, 3.52, and 4.57 µm. The experimental results are presented in Fig. 7(c). The position of the integrated dispersion equal to zero is basically consistent with the dispersive wave generation wavelength. Small differences in DW position can be attributed to deviations in actual waveguide dimensions from simulations due to waveguide manufacturing tolerances. It is observed that as the waveguide width increases, the DW near 2 µm moves towards longer wavelengths, and the BPM SHG signal near 1 µm also exhibits a similar shift in the long-wavelength direction. Accordingly, the wavelengths of the sum frequency process between the soliton and the dispersive wave also move towards the long wavelengths.

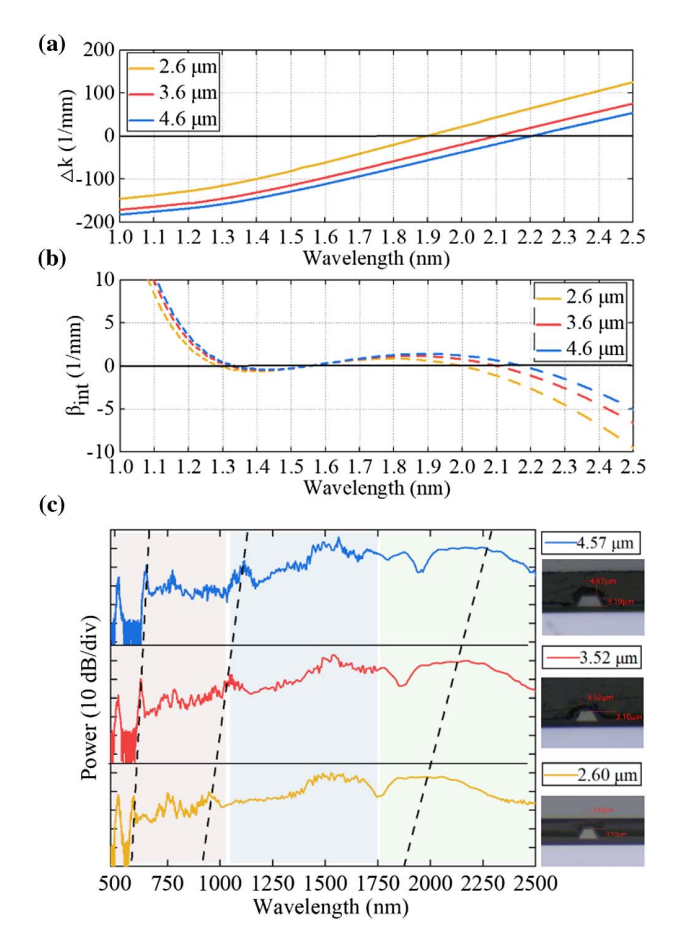


Fig. 7. SCG in MgO:LNOI micro-waveguides of different top-widths. (a) Simulation results of integrated dispersion β_{int} for different top-width waveguides. (b) Simulation results of SHG phase mismatch Δk. (c) Experimentally measured SCG spectra in the 2.60-μm, 3.52-μm, and 4.57-μm top-width waveguides.

APPENDIX B: COMPARISON OF SCG PERFORMANCE ON VARIOUS PLATFORMS

The detailed comparison of our work on SCG with similar studies on various integrated photonics platforms is shown

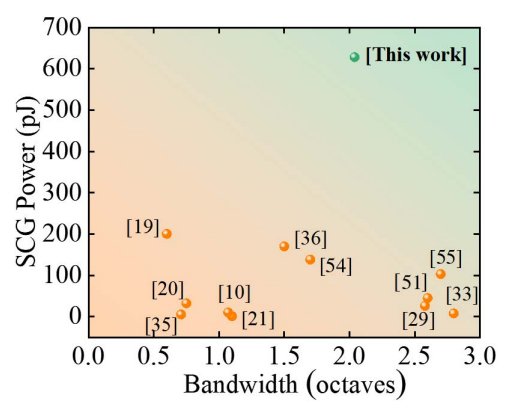


Fig. 8. Comparison of SCG bandwidth and power on various integrated photonics platforms.

in Table 1. A comparison of two critical metrics for evaluating SCG performance, namely, output power and bandwidth, is illustrated in Fig. 8. It can be found that our LNOI microwaveguide configuration achieves comparable conversion bandwidth, yet with much higher achievable power. The waveguide lengths are no longer constrained by process limitations. The extended waveguide lengths ensure enhanced nonlinearity, and it has significant advantages in overall transmittance and fiber compatibility, thereby facilitating high-power SCG.

Funding. National Key Research and Development Program of China (2022YFA1205100, 2023YFA1407200); National Natural Science Foundation of China (12192252, 12074252); Science and Technology Commission of Shanghai Municipality (24JD1401700); Shanghai Municipal Science and Technology Major Project (2019SHZDZX01-ZX06); Innovation Program for Quantum Science and Technology (2021ZD0300802); Yangyang Development Fund.

Disclosures. The authors declare no conflicts of interest.

Table 1. Comparison of SCG Performance in Waveguides on Different Platforms

Platform	Length (mm)	Insertion Loss (dB)	Input Pump Energy (pJ)	SCG Output Energy (pJ)	Overall Efficiency ^a	Bandwidth (Octaves)	Ref.
Si ₃ N ₄ nano-waveguide	15	6.7	650	138	21%	1.7	[54]
AlN nano-waveguide	6	17.3	1719	32	1.9%	0.75	[20]
AlN nano-waveguide	10	8	800	103	12.8%	2.7	[55]
Silicon nano-waveguide	10	25.4	347	1	0.3%	1.1	[21]
LNOI nano-waveguide	5	17.5	562	10	1.8%	1.07	[10]
LNOI nano-waveguide	5	17	1303	26	2.0%	2.58	[29]
CPPLN nano-waveguide	6.6	20.7	893	7.6	0.9%	2.8	[33]
LNOI nano-waveguide	14	22.4	869	5	0.6%	0.71	[35]
LNOI nano-waveguide	10	13.2	3552	170	4.8%	1.5	[36]
LNOI nano-waveguide	5	18.2	3000	45	1.5%	2.6	[51]
LNOI micro-waveguide	20	3.4	1375	628	45.7%	2.04	Ours

[&]quot;Overall conversion efficiency in which the device insertion loss is considered.

Data Availability. The data that support the findings of this study are available from the corresponding author upon reasonable request.

REFERENCES

- A. L. Gaeta, M. Lipson, and T. J. Kippenberg, "Photonic-chip-based frequency combs," Nat. Photonics 13, 158–169 (2019).
- S. A. Diddams, K. Vahala, and T. Udem, "Optical frequency combs: coherently uniting the electromagnetic spectrum," Science 369, eaay3676 (2020).
- T. Fortier and E. Baumann, "20 years of developments in optical frequency comb technology and applications," Commun. Phys. 2, 153 (2019).
- S. B. Papp, K. Beha, P. Del'Haye, et al., "Microresonator frequency comb optical clock," Optica 1, 10–14 (2014).
- D. Grassani, E. Tagkoudi, H. Guo, et al., "Mid infrared gas spectroscopy using efficient fiber laser driven photonic chip-based supercontinuum," Nat. Commun. 10, 1553 (2019).
- H. Hu and L. K. Oxenløwe, "Chip-based optical frequency combs for high-capacity optical communications," Nanophotonics 10, 1367– 1385 (2021).
- T. Udem, R. Holzwarth, and T. W. Hänsch, "Optical frequency metrology," Nature 416, 233–237 (2002).
- V. Brasch, M. Geiselmann, T. Herr, et al., "Photonic chip-based optical frequency comb using soliton Cherenkov radiation," Science 351, 357–360 (2016).
- 9. L. Chang, S. Liu, and J. E. Bowers, "Integrated optical frequency comb technologies," Nat. Photonics 16, 95–108 (2022).
- Y. Okawachi, M. Yu, B. Desiatov, et al., "Chip-based self-referencing using integrated lithium niobate waveguides," Optica 7, 702–707 (2020).
- 11. J. M. Dudley, G. Genty, and S. Coen, "Supercontinuum generation in photonic crystal fiber," Rev. Mod. Phys. **78**, 1135–1184 (2006).
- A. Blanco-Redondo, C. M. Sterkede, C. Xu, et al., "The bright prospects of optical solitons after 50 years," Nat. Photonics 17, 937
 942 (2023).
- 13. S. Mosca, I. Ricciardi, M. Parisi, *et al.*, "Direct generation of optical frequency combs in $\chi^{(2)}$ nonlinear cavities," Nanophotonics **5**, 316–331 (2016).
- C. Tang, M. Nie, J. Chen, et al., "Broadband frequency comb generation through cascaded quadratic nonlinearity in thin-film lithium niobate microresonators," Opt. Lett. 49, 2449–2452 (2024).
- B. B. Zhou, X. Liu, H. R. Guo, et al., "Parametrically tunable solitoninduced resonant radiation by three-wave mixing," Phys. Rev. Lett. 118, 143901 (2017).
- A. V. Husakou and J. Herrmann, "Supercontinuum generation of higher-order solitons by fission in photonic crystal fibers," Phys. Rev. Lett. 87, 203901 (2001).
- I. Hartl, G. Imeshev, M. E. Fermann, et al., "Integrated self-referenced frequency-comb laser based on a combination of fiber and waveguide technology," Opt. Express 13, 6490–6496 (2005).
- K. Hitachi, A. Ishizawa, T. Nishikawa, et al., "Carrier-envelope offset locking with a 2f-to-3f self-referencing interferometer using a dualpitch PPLN ridge waveguide," Opt. Express 22, 1629–1635 (2014).
- H. Guo, C. Herkommer, A. Billat, et al., "Mid-infrared frequency comb via coherent dispersive wave generation in silicon nitride nanophotonic waveguides," Nat. Photonics 12, 330–335 (2018).
- X. Liu, A. W. Bruch, J. Lu, et al., "Beyond 100 THz-spanning ultraviolet frequency combs in a non-centrosymmetric crystalline waveguide," Nat. Commun. 10, 2971 (2019).
- B. Kuyken, T. Ideguchi, S. Holzner, et al., "An octave-spanning midinfrared frequency comb generated in a silicon nanophotonic wire waveguide," Nat. Commun. 6, 6310 (2015).
- H. Guo, W. Weng, J. Liu, et al., "Nanophotonic supercontinuum-based mid-infrared dual-comb spectroscopy," Optica 7, 1181–1188 (2020).
- M. H. P. Pfeiffer, C. Herkommer, J. Liu, et al., "Octave-spanning dissipative Kerr soliton frequency combs in Si₃N₄ microresonators," Optica 4, 684–691 (2017).

- X. Liu, Z. Gong, A. W. Bruch, et al., "Aluminum nitride nanophotonics for beyond-octave soliton microcomb generation and self-referencing," Nat. Commun. 12, 5428 (2021).
- A. Roy, L. Ledezma, L. Costa, et al., "Visible-to-mid-IR tunable frequency comb in nanophotonics," Nat. Commun. 14, 6549 (2023).
- D. Zhu, L. Shao, M. Yu, et al., "Integrated photonics on thin-film lithium niobate," Adv. Opt. Photonics 13, 242–352 (2021).
- M. G. Vazimali and S. Fathpour, "Applications of thin-film lithium niobate in nonlinear integrated photonics," Adv. Photonics 4, 034001 (2022).
- J. Lin, F. Bo, Y. Cheng, et al., "Advances in on-chip photonic devices based on lithium niobate on insulator," Photonics Res. 8, 1910–1936 (2020).
- M. Yu, B. Desiatov, Y. Okawachi, et al., "Coherent two-octavespanning supercontinuum generation in lithium-niobate waveguides," Opt. Lett. 44, 1222–1225 (2019).
- 30. V. Brasch, E. Lucas, J. D. Jost, et al., "Self-referenced photonic chip soliton Kerr frequency comb," Light Sci. Appl. 6, e16202 (2017).
- D. J. Jones, S. A. Diddams, J. K. Ranka, et al., "Carrier-envelope phase control of femtosecond mode-locked lasers and direct optical frequency synthesis," Science 288, 635–639 (2000).
- A. S. Mayer, A. Klenner, A. R. Johnson, et al., "Frequency comb offset detection using supercontinuum generation in silicon nitride waveguides," Opt. Express 23, 15440–15451 (2015).
- T. H. Wu, L. Ledezma, C. Fredrick, et al., "Visible-to-ultraviolet frequency comb generation in lithium niobate nanophotonic waveguides," Nat. Photonics 18, 218–223 (2024).
- M. Jankowski, C. Langrock, B. Desiatov, et al., "Ultrabroadband nonlinear optics in nanophotonic periodically poled lithium niobate waveguides," Optica 7, 40–46 (2020).
- M. Escalé Reig, F. Kaufmann, H. Jiang, et al., "Generation of 280 THz-spanning near-ultraviolet light in lithium niobate-on-insulator waveguides with sub-100 pJ pulses," APL Photonics 5, 121301 (2020).
- J. Lu, J. B. Surya, X. Liu, et al., "Octave-spanning supercontinuum generation in nanoscale lithium niobate waveguides," Opt. Lett. 44, 1492–1495 (2019).
- P. K. Chen, I. Briggs, C. Cui, et al., "Adapted poling to break the nonlinear efficiency limit in nanophotonic lithium niobate waveguides," Nat. Nanotechnol. 19, 44–50 (2024).
- C. S. Brès, A. Della Torre, D. Grassani, et al., "Supercontinuum in integrated photonics: generation, applications, challenges, and perspectives," Nanophotonics 12, 1199–1244 (2023).
- C. Wang, C. Langrock, A. Marandi, et al., "Ultrahigh-efficiency wavelength conversion in nanophotonic periodically poled lithium niobate waveguides," Optica 5, 1438–1441 (2018).
- R. Luo, Y. He, H. Liang, et al., "Highly tunable efficient second-harmonic generation in a lithium niobate nanophotonic waveguide," Optica 5, 1006–1011 (2018).
- L. He, M. Zhang, A. Shams-Ansari, et al., "Low-loss fiber-to-chip interface for lithium niobate photonic integrated circuits," Opt. Lett. 44, 2314–2317 (2019).
- X. Liu, S. Gao, C. Zhang, et al., "Ultra-broadband and low-loss edge coupler for highly efficient second harmonic generation in thin-film lithium niobate," Adv. Photonics Nexus 1, 016001 (2022).
- Y. Wu, J. Wei, S. Tao, et al., "Efficient yellow and green lasers generation in lithium niobate micro-waveguides," IEEE Photonics Technol. Lett. 37, 901–904 (2025).
- Y. Zhang, H. Li, T. Ding, et al., "Scalable, fiber-compatible lithium-niobate-on-insulator micro-waveguides for efficient nonlinear photonics," Optica 10, 688–693 (2023).
- T. Ding, Y. Tang, H. Li, et al., "Noncritical birefringence phasematched second harmonic generation in a lithium-niobate-oninsulator micro-waveguide for green light emission," Opt. Lett. 49, 1121–1124 (2024).
- C. Lu, H. Li, J. Qiu, et al., "Second and cascaded harmonic generation of pulsed laser in a lithium niobate on insulator ridge waveguide," Opt. Express 30, 1381–1387 (2022).
- Y. Tang, T. Ding, Y. Zhang, et al., "Octave-spanning second-harmonic generation in dispersion engineered lithium niobate-on-insulator micro-waveguide," Adv. Photonics Res. 5, 2400051 (2024).

- 48. D. Zheng, Y. Kong, S. Liu, et al., "The simultaneous enhancement of photorefraction and optical damage resistance in MgO and Bi₂O₃ codoped LiNbO₃ crystals," Sci. Rep. 6, 20308 (2016).
- L. Zhao, L. Shi, J. Wang, et al., "Effect of doping Mg on the structure and optical properties of LiNbO₃ films prepared by radio-frequency magnetron sputtering," Mater. Sci. Semicond. Process. 108, 104901 (2020).
- C. R. Phillips, C. Langrock, J. S. Pelc, et al., "Supercontinuum generation in quasi-phase-matched waveguides," Opt. Express 19, 18754–18773 (2011).
- M. Hamrouni, M. Jankowski, A. Y. Hwang, et al., "Picojoule-level supercontinuum generation in thin-film lithium niobate on sapphire," Opt. Express 32, 12004–12011 (2024).
- M. Conforti, F. Baronio, and C. De Angelis, "Nonlinear envelope equation for broadband optical pulses in quadratic media," Phys. Rev. A 81, 053841 (2010).
- C. R. Phillips, M. Jankowski, N. Flemens, et al., "General framework for ultrafast nonlinear photonics: unifying single and multi-envelope treatments [Invited]," Opt. Express 32, 8284–8307 (2024).
- D. D. Hickstein, G. C. Kerber, D. R. Carlson, et al., "Quasi-phase-matched supercontinuum generation in photonic waveguides," Phys. Rev. Lett. 120, 053903 (2018).
- D. D. Hickstein, H. Jung, D. R. Carlson, et al., "Ultrabroadband supercontinuum generation and frequency-comb stabilization using on-chip waveguides with both cubic and quadratic nonlinearities," Phys. Rev. Appl. 8, 014025 (2017).